

INFRARED ARRAY CAMERA (IRAC) COLORS OF YOUNG STELLAR OBJECTS

LORI E. ALLEN,¹ NURIA CALVET,¹ PAOLA D’ALESSIO,² BRUNO MERIN,³ LEE HARTMANN,¹ S. THOMAS MEGEATH,¹
 ROBERT A. GUTERMUTH,⁴ JAMES MUZEROLLE,⁵ JUDITH L. PIPHER,⁴ PHILIP C. MYERS,¹ AND GIOVANNI G. FAZIO¹

Received 2004 March 26; accepted 2004 May 20

ABSTRACT

We compare the infrared colors predicted by theoretical models of protostellar envelopes and protoplanetary disks with initial observations of young stellar objects made with the Infrared Array Camera (IRAC) on the *Spitzer Space Telescope*. Disk and envelope models characterized by infall and/or accretion rates found in previous studies can quantitatively account for the range of IRAC colors found in four young embedded clusters: S140, S171, NGC 7129, and Cep C. The IRAC color-color diagram ([3.6]–[4.5] vs. [5.8]–[8.0]) can be used to help distinguish between young stars with only disk emission and protostars with circumstellar envelopes.

Subject headings: infrared: stars — stars: formation — stars: pre-main-sequence

1. INTRODUCTION

It has now been several decades since the first observations of infrared (IR) excess emission from young stars (Mendoza 1966, 1968). The excess emission is well above that expected from reddened stellar photospheres and originates from the dusty circumstellar disks and envelopes surrounding young stars. For these reasons, IR color-color diagrams have proven to be excellent tools for identifying and classifying young stellar objects. In general, young stars are found in three regions in the near-IR (*JHKL*) diagrams. Objects with accretion disks (Class II) fall on the classical T Tauri (CTT) locus or along the reddened CTT locus, and objects whose emission is dominated by infalling envelopes (Class I) fall redward of the reddened CTT locus. Stars having disks with large inner holes are found in the region corresponding to reddened main-sequence stars (Meyer et al. 1997). In an exhaustive study of star formation in the Taurus molecular cloud, Kenyon & Hartmann (1995) combined ground-based near-IR photometry with *IRAS* fluxes to derive spectral indices for Class I and II sources and to show that there is a smooth progression in IR colors from disk-dominated Class II to envelope-dominated Class I. They, along with others (Lada et al. 2000) also showed that the *K*–*L* color index is a more effective measure of near-IR excess than *H*–*K* and is better for distinguishing Class I from Class II sources.

The Infrared Array Camera (IRAC) on *Spitzer* (Werner et al. 2004; Fazio et al. 2004) has the potential to extend our understanding of disk evolution and star formation by detecting optically obscured, deeply embedded young stars and protostars, the emission from their disks, and, at earlier stages, from their infalling envelopes. The great advantage of IRAC over ground-based telescopes is its sensitivity in the

3–8 μm bands that contain relatively little contribution from stellar photospheres as compared to disks and envelopes. It is important that we understand this new color space and how to use it to identify young stars of various evolutionary classes. This contribution presents a preliminary interpretation of the IRAC color-color diagram, using predictions of existing models for disks and envelopes and adopting values for parameters which are well understood from star formation studies of nearby regions like the Taurus molecular cloud. These models define clearly separated regions in the IRAC color-color diagram. IRAC observations of four young clusters (Megeath et al. 2004) are consistent with the model predictions.

2. MODELS

Models in the disk grid were calculated according to the procedures of D’Alessio et al. (1998, 1999, 2001). In brief, the disk is assumed to be steadily accreting at a rate \dot{M} onto a star of age t , mass M , radius R , and effective temperature T_{eff} . The material in the disk consists of gas and dust, with the standard mass ratio ($M_{\text{dust}}/M_{\text{gas}} = 10^{-2}$), well mixed and uniformly distributed. The dust mixture is that proposed by Pollack et al. (1994) and has a size distribution $n(a)da \propto a^{-p}da$ between limiting sizes a_{min} and a_{max} . The disk is heated by viscous dissipation and by irradiation from the central object, and viscosity is calculated with the α prescription (Shakura & Sunyaev 1973). Models are truncated at the dust destruction radius R_{rim} , where the disk is frontally illuminated by the central object, because gas inside R_{rim} is optically thin (P. D’Alessio et al. 2004, in preparation). The truncation radius is set by the sum of the stellar and accretion luminosity (Muzerolle et al. 2003), and the dust destruction temperature is set at 1400 K, the sublimation temperature of silicates at characteristic densities of the inner disk. The wall at R_{rim} , which has a fixed height of four scale heights, emits as a blackbody at this temperature (Natta et al. 2001; Muzerolle et al. 2003; P. D’Alessio 2004, in preparation). The equations of disk structure are solved including these heating sources to yield the detailed radial-vertical structure. The emerging spectral energy distribution (SED) is calculated by ray-by-ray integration of the transfer equation for each line of sight. Using these procedures, we have constructed an extensive grid of disk models that cover the following range of parameter space: $T_{\text{eff}} = 4000\text{--}10,000$ K for

¹ Harvard-Smithsonian Center for Astrophysics, 60 Garden Street, Cambridge, MA 02138; allen@cfa.harvard.edu.

² Centro de Radioastronomía y Astrofísica, Apdo. Postal 72-3 (Xangari), 58089 Morelia, Michoacán, Mexico.

³ Laboratorio de Astrofísica Espacial y Física Fundamental, (INTA), Apartado de Correos 50727, 28080 Madrid, Spain.

⁴ Department of Physics and Astronomy, University of Rochester, Rochester, NY 14627-0171.

⁵ Steward Observatory, University of Arizona, 933 North Cherry Avenue, Tucson, AZ 85721.

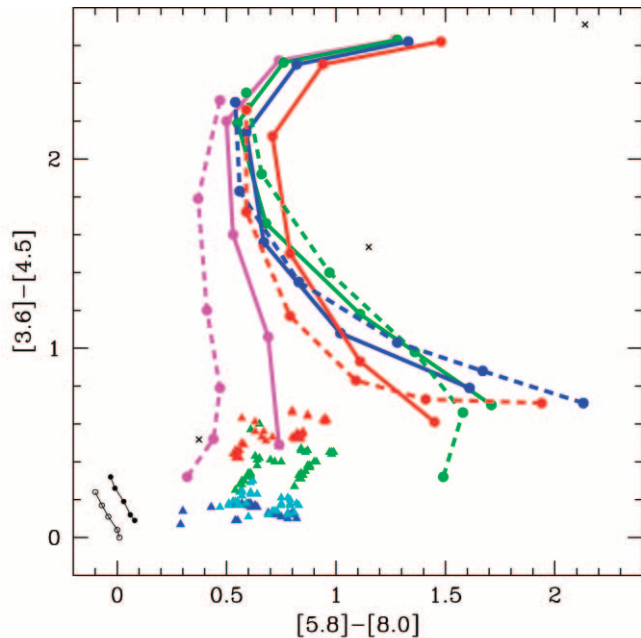


FIG. 1.—IRAC colors for disk models (triangles) and envelope models (circles). Disk models assume $T_{\text{eff}} = 4000$ K, $t = 1$ Myr. Disk accretion rates are color coded: dark blue, light blue, green, and red represent $\log \dot{M} = -9$, -8 , -7 , -6 $M_{\odot} \text{ yr}^{-1}$, respectively. Models are plotted for two values of p (2.5, 3.5) and six values of a_{max} (1 μm , 10 μm , 100 μm , 1 mm, 1 cm, and 10 cm). The two inclinations (30° and 60°) form discernible loci centered at $[5.8] - [8.0] = 0.6$ and 0.9 . Envelope models are shown for a range of central source luminosities, color coded as magenta, green, blue, and red for 0.1, 1, 10, and 100 L_{\odot} , respectively. Envelope densities are shown for $\log \rho_1 = -14$, -13.5 , -13.35 , -13 , -12.75 , and -12.5 g cm^{-3} , increasing from bottom to top. Models are plotted for two values of R_c , 50 AU (solid line) and 300 AU (dashed line), and one inclination (60°). For comparison, blackbody colors ($T = 300$, 500, and 1200 K) are plotted by crosses. Two blackbodies with extinctions of $A_v = 0$, 5, 10, 15, and 20 mag are shown; open circles correspond to a blackbody of $T = 10,000$ K and filled circles to $T = 4000$ K.

1 and 10 Myr old stars, $\log \dot{M} = -9$ to -6 $M_{\odot} \text{ yr}^{-1}$, disk radii $R_d = 100$ and 300 AU, $p = 2.5$, 3.5, $a_{\text{max}} = 1$ – 10^5 μm , and inclinations 30° and 60° , with fixed $a_{\text{min}} = 0.005$ μm and $\alpha = 0.01$. Details of the grid will be published elsewhere (D'Alessio et al. 2004). Here we present only those models for $T_{\text{eff}} = 4000$ K, $t = 1$ Myr.

Models in the Class I grid were calculated following the procedures of Kenyon et al. (1993, hereafter KCH93) and Calvet et al. (1994). The slowly rotating infalling envelope structure of Terebey et al. (1984) has been adopted; in this model, the envelope is nearly spherically symmetric at radii much larger than the centrifugal radius R_c and departs from spherical symmetry at radii less than R_c , where material falls onto the disk. The heating of the matter in the envelope with density distribution $\rho(r, \theta)$ is set by the luminosity of the central object L . The temperature is calculated from the radiative equilibrium condition using the angle-averaged density, and the inclination-dependent flux is calculated from ray-by-ray integration of the transfer equation using the angle-dependent density. The scattering component of the source function in the flux calculation has been taken as the sum of the direct and the diffuse mean intensity, following Calvet et al. (1994). Class I models were calculated for $L = 0.1$, 1, 10, and 100 L_{\odot} , $\log \rho_1 = -14$, -13.5 , -13.35 , -13 , -12.75 , and -12.5 g cm^{-3} , where ρ_1 is the density at 1 AU of the equivalent spherically symmetric envelope (see KCH93), and $R_c = 50$ and 300 AU. Model colors shown have been calculated for an inclination of 60° .

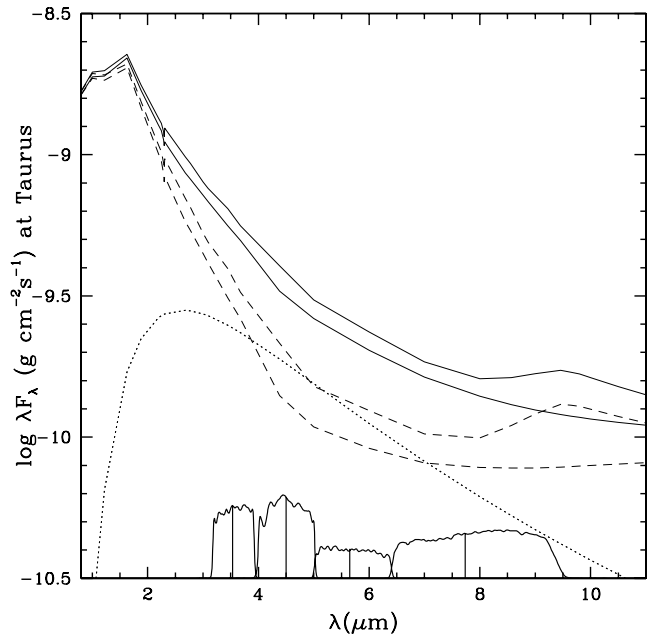


FIG. 2.—Representative SEDs for a disk model with an inclination of 60° , $\dot{M} = 10^{-8}$ $M_{\odot} \text{ yr}^{-1}$, and two values of a_{max} , 0.1 μm (upper lines) and 1 mm (lower lines). The solid lines show the total emission (star+disk+wall), the dashed lines show the emission from the star+disk, and the dotted line shows the emission from the wall, modeled as a 1400 K blackbody. Spectral response curves for the IRAC bands (normalized to an arbitrary value) are shown at the bottom, and the band effective wavelengths are indicated (vertical lines). The wall contributes significantly to the total emission, especially in the IRAC bands.

Model colors were calculated by convolving the model SED with the IRAC filter response functions and by using the Vega fluxes in the IRAC bands as photometric zero points. The resulting magnitudes are thus referenced to the Vega system (as are the measured magnitudes of the embedded cluster sample). Figure 1 shows IRAC colors from grids of disk (Class II) and infalling-envelope (Class I) models. The models cover the range of parameters typical of young stellar objects.

3. DISCUSSION

3.1. Disk Models

The novel element introduced in the disk models presented here is the emission of the disk wall at the dust sublimation radius. A sharp transition in the disk where dust sublimates, illuminated directly by the star, was presented as the explanation for the near-IR SEDs of Herbig Ae/Be stars by Natta et al. (1999). Muzerolle et al. (2003) found similar excesses in classical T Tauri stars and realized that for these low-luminosity objects, the accretion luminosity L_{acc} emitted by the accretion shock on the stellar surface must be included when finding the dust-sublimation radius.

Figure 2 shows the SEDs for a representative model. The wall contribution plays a substantial role in the IRAC wavelength range and results in a relatively compact region in the $[5.8] - [8.0]$ versus $[3.6] - [4.5]$ color plane, as shown by the triangles in Figure 1.

The spread in the $[3.6] - [4.5]$ color is dominated by accretion rate; sources with higher \dot{M} are redder in $[3.6] - [4.5]$. This behavior is due to an increase of both the disk emission and the wall emission as \dot{M} increases. As the accretion rate rises, there is an increase in viscous dissipation, resulting in higher

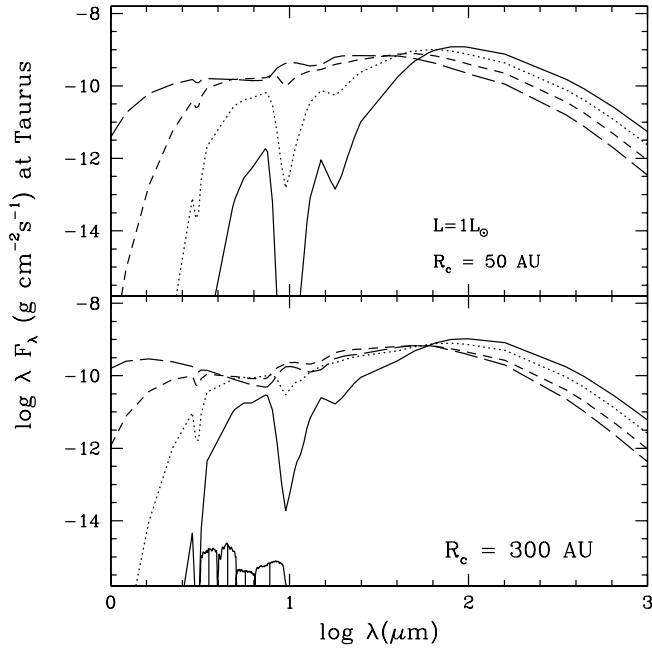


FIG. 3.—Representative SEDs for envelope models with $L = 1 L_{\odot}$ and $R_e = 50$ AU (upper panel) and $R_e = 300$ AU (lower panel) and for densities $\log \rho_1 = -14, -13.5, -13$, and -12.5 g cm^{-3} , increasing from top to bottom. As in the previous figure, IRAC bandpasses are indicated.

disk fluxes. In addition, the increase in L_{acc} results in more energy irradiating the wall; as a result, the dust-sublimation radius moves outward, and the wall emitting area increases (Muzerolle et al. 2003). Although not shown here for economy of space, we note that the wall emission becomes increasingly dominant as the stellar luminosity increases, and so does the wall emitting area. In fact, for stellar properties corresponding to Herbig Ae/Be stars, for which $L_* > L_{\text{acc}}$, the predicted $[3.6] - [4.5]$ color is approximately constant, ~ 0.4 , equal to that of the blackbody at $T = 1400$ K, the assumed dust-destruction temperature.

Disk emission is more conspicuous in the $[5.8] - [8.0]$ color, as shown in Figure 2, and therefore disk properties such as grain size and \dot{M} play a larger role in determining the spread. For instance, the disk contribution decreases as a_{max} increases, because the disk becomes less flared (D'Alessio et al. 2001). As a result, the $[5.8] - [8.0]$ color becomes bluer. Another source of spread is inclination. The two inclinations plotted in Figure 1 (30° and 60°) form discernible loci, with the higher-inclination sources redward of the lower ones. Although a Class II source with an extremely high inclination (i.e., edge-on) may lie blueward of this region (reflecting the scattered stellar component), most of the inclination-dependent behavior of the models is encompassed in the region plotted.

3.2. Envelope Models

Envelope models (plotted as circles in Fig. 1) span a larger space in both $[3.6] - [4.5]$ and $[5.8] - [8.0]$ colors compared to disk models. To understand the color behavior in a schematic way consider Figure 3, which shows model SEDs. An increase in density in the envelope results in a shift of the $\tau \sim 1$ surface further out in the envelope (see Appendix in KCH93; Hartmann 1998). As a result, the overall SED shifts toward longer wavelengths, and the $[3.6] - [4.5]$ colors become rapidly redder with increasing density. In addition, as the amount of material in the envelope increases, absorption increases,

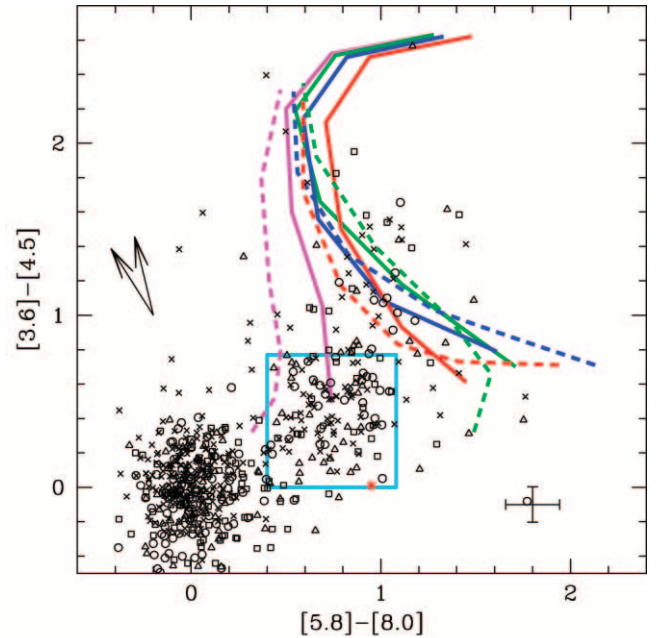


FIG. 4.—Model colors from Fig. 1 and measured IRAC colors for S140 (squares), Cep C (crosses), S171 (circles), and NGC 7129 (triangles) from the IRAC Guaranteed Time Observer (GTO) embedded clusters survey (Megeath et al. 2004). Representative error bars, including average photometric uncertainties and an estimated 10% uncertainty in the absolute flux calibration, are shown. The light blue square delineates the approximate domain of Class II sources, and the colored lines show the Class I models as in Fig. 1. The red asterisk marks the IRAC colors of TW Hya (L. Hartmann et al. 2004, in preparation), a 10 Myr old star with a disk (Muzerolle et al. 2000). Extinction vectors are shown for $A_v = 30$ mag, using the two extremes of the six vectors calculated by Megeath et al. (2004). The vector on the left is for a flat-spectrum source and Draine & Lee (1984) extinction law, while the vector to the right is for a Vega spectrum and the extinction law of Mathis (1990).

and the silicate feature at $\sim 10 \mu\text{m}$ becomes deeper. The $[5.8] - [8.0]$ color becomes first bluer, as the flux in $[8.0]$, contaminated by the silicate feature, decreases faster than the flux in the $[5.8]$ band. As density continues to increase, this situation reverses, and the $[5.8] - [8.0]$ color becomes redder.

As shown in the bottom panel of Figure 3, an increase in R_e , which implies clearing of the inner envelope, is equivalent in the near- to mid-IR to a decrease in density. As a result, the $[3.6] - [4.5]$ color becomes bluer, and so does the $[5.8] - [8.0]$ color for high values of ρ_1 . However, for low ρ_1 , the silicate feature turns into emission, making the $[5.8] - [8.0]$ color redder (Fig. 1).

The color behavior as a function of ρ_1 and R_e does not depend strongly on source luminosity. However, as shown in Figure 2 of KCH93, the strength of the silicate absorption feature decreases as luminosity increases. At high values of ρ_1 , the $[5.8] - [8.0]$ colors are less affected by the silicate absorption and do not get as blue as L increases. At low densities, the extinguished spectrum of the central object begins to contribute along with envelope emission in the IRAC bands, which tends to make the color bluer; a competing effect is the increase in strength of the silicate emission, which makes $[5.8] - [8.0]$ redder. For $L = 0.1 L_{\odot}$, the second effect is negligible so colors are very blue (Fig. 1).

Other effects not included in this preliminary modeling effort, such as degree of flattening of the envelope or the presence of outflow cavities, may change the colors as well, especially at low densities. For example, Whitney et al. (2003) predicted IRAC colors for a range of protostellar (Class 0 and

I) and T Tauri objects (Class II). Their calculations for Class II objects span a much smaller range in the color-color diagram, because they considered a much smaller range of parameter space than we have here, and they did not include the effects of a hot inner disk wall. The objects Whitney et al. label as Class I have predicted colors that are considerably bluer than we infer here, and the region populated by Class 0 sources in the Whitney et al. calculations overlaps with the region of Taurus Class I sources (L. Hartmann et al. 2004, in preparation). The discrepancy appears to be the result of the particular outflow cavities adopted by Whitney et al., which greatly reduce the amount of dust close to the central source and thus strongly reduce the extinction and dust thermal emission in the 3–8 μm region (see Osorio et al. 2003 for a related discussion).

3.3. Comparison with Observed Colors

Figure 4 shows measured IRAC colors of four young clusters (Megeath et al. 2004; Gutermuth et al. 2004) and for comparison, the loci of the models presented in Figure 1. The data seem to cluster into three main regions: a clump around (0, 0) that contains mostly background/foreground stars and Class III sources with no intrinsic IR excess, a clump that occupies the Class II region (within the large blue box), and a group that runs along the Class I locus with $L \geq 1 L_{\odot}$. Sources that lie between the [5.8]–[8.0] colors of stellar photospheres and Class III stars (~ 0) and Class II sources (≥ 0.4) can be understood if the height of the wall at R_{rim} was less than assumed here, because of the effects of dust grain growth and settling. In addition, there are a few sources that do not lie inside the Class II locus but *do* lie along the extinction vector and could therefore be reddened Class II objects. The most extreme of these, near [5.8]–[8.0] = 0, [3.6]–[4.5] = 1.5, are coincident with filaments of high opacity (dark even at 8 μm), consistent with the large A_v implied by this scenario. Alternatively, they could be extremely low luminosity Class I sources.

The common definition of Class I and II sources is that they have positive or negative spectral indices, respectively, in λF_{λ} ; thus, the approximate boundary between Class I and II should lie approximately at [3.6] – [4.5] ~ 0.7 and [5.8] – [8.0] ~ 1 . The model predictions presented here are in agreement with this boundary. As discussed, features in the SED, notably the silicate feature at $\sim 10 \mu\text{m}$, have a large effect on the [5.8]–[8.0] color, producing some exceptions to this rule. In addition, the [3.6]–[4.5] colors of low-density envelopes are very sensitive to the nature of the central objects contained within. For example, low-density envelopes around stars with disks would have [3.6]–[4.5] colors near the Class II locus.

4. SUMMARY

The IRAC color-color diagram ([3.6]–[4.5] vs. [5.8]–[8.0]) is a useful tool for identifying young stars having IR excess emission. While there is some overlap between low-density, low-luminosity Class I sources and Class II sources, the classes are otherwise well segregated. The distribution of measured IRAC colors of sources in four young clusters is consistent with the distribution of model colors. Confirmation of this color-color diagram as a powerful diagnostic tool awaits a more detailed comparison to the observed colors of well-characterized individual sources.

This work is based on observations made with the *Spitzer* Space Telescope, which is operated by the Jet Propulsion Laboratory, California Institute of Technology, under NASA contract 1407. Support for this work was provided by NASA through contract 1256790 issued by JPL/Caltech. This work was supported in part by grant AR-09524.01-A from the Space Telescope Science Institute and by NASA Origins of Solar Systems grant NAG5-9670.

REFERENCES

- Calvet, N., Hartmann, L., Kenyon, S. J., & Whitney, B. A. 1994, *ApJ*, 434, 330
D'Alessio, P. 2004, IAU Symp. 221, *Star Formation at High Angular Resolution*, ed. M. Burton, R. Jayawardhana, & T. Bourke (San Francisco: ASP), 256
D'Alessio, P., Calvet, N., & Hartmann, L. 2001, *ApJ*, 553, 321
D'Alessio, P., Calvet, N., Hartmann, L., Lizano, S., & Cantó, J. 1999, *ApJ*, 527, 893
D'Alessio, P., Cantó, J., Calvet, N., & Lizano, S. 1998, *ApJ*, 500, 411
Draine, B. T., & Lee, H. M. 1984, *ApJ*, 285, 89
Fazio, G. G., et al. 2004, *ApJS*, 154, 10
Gutermuth, R. A., Megeath, S. T., Muzerolle, J., Allen, L. E., Pipher, J. L., Myers, P. C., & Fazio, G. G. 2004, *ApJS*, 154, 374
Hartmann, L. 1998, *Accretion Processes in Star Formation* (Cambridge: Cambridge Univ. Press)
Kenyon, S. J., Calvet, N., & Hartmann, L. 1993, *ApJ*, 414, 676 (KCH93)
Kenyon, S. J., & Hartmann, L. 1995, *ApJS*, 101, 117
Lada, C. J., Muench, A. A., Haisch, K. E., Jr., Lada, E. A., Alves, J. F., Tollestrup, E. V., & Willner, S. P. 2000, *AJ*, 120, 3162
Mathis, J. S. 1990, *ARA&A*, 28, 37
Megeath, S. T., Gutermuth, R. A., Allen, L. E., Pipher, J. L., Myers, P. C., & Fazio, G. G. 2004, *ApJS*, 154, 367
Mendoza V., E. E. 1966, *ApJ*, 143, 1010
———. 1968, *ApJ*, 151, 977
Meyer, M. R., Calvet, N., & Hillenbrand, L. A. 1997, *AJ*, 114, 288
Muzerolle, J., Calvet, N., Briceño, C., Hartmann, L., & Hillenbrand, L. 2000, *ApJ*, 535, L47
Muzerolle, J., Calvet, N., Hartmann, L., & D'Alessio, P. 2003, *ApJ*, 597, L149
Natta, A., Prusti, T., Neri, R., Thi, W. F., Grinin, V. P. & Mannings, V. 1999, *A&A*, 350, 541
Natta, A., Prusti, T., Neri, R., Wooden, D., Grinin, V. P., & Mannings, V. P. 2001, *A&A*, 371, 186
Osorio, M., D'Alessio, P., Muzerolle, J., Calvet, N., & Hartmann, L. 2003, *ApJ*, 586, 1148
Pollack, J. B., Hollenbach, D., Beckwith, S., Simonelli, D. P., Roush, T., & Fong, W. 1994, *ApJ*, 421, 615
Shakura, N. I., & Sunyaev, R. A. 1973, *A&A*, 24, 337
Terebey, S. Shu, F. H., & Cassen, P. 1984, *ApJ*, 286, 529
Werner, M. W., et al. 2004, *ApJS*, 154, 1
Whitney, B. A., Wood, K. A., Bjorkman, J. E., & Cohen, M. 2003, *ApJ*, 598, 1079